# Proximity-induced Majorana hinge modes in antiferromagnetic topological insulators

Yang Peng[1,2,*] and Yong Xu[3,4,5,†]

[1] *Institute of Quantum Information and Matter and Department of Physics, California Institute of Technology, Pasadena, CA 91125, USA*
[2] *Walter Burke Institute for Theoretical Physics, California Institute of Technology, Pasadena, CA 91125, USA*
[3] *State Key Laboratory of Low Dimensional Quantum Physics, Department of Physics, Tsinghua University, Beijing 100084, Peoples Republic of China*
[4] *Collaborative Innovation Center of Quantum Matter, Beijing 100084, Peoples Republic of China*
[5] *RIKEN Center for Emergent Matter Science (CEMS), Wako, Saitama 351-0198, Japan*

We propose a realization of chiral Majorana modes propagating on the hinges of a 3D antiferromagnetic topological insulator, which was recently theoretically predicted and experimentally confirmed in the tetradymite-type $MnBi_2Te_4$-related ternary chalgogenides. These materials consist of ferromagnetically ordered 2D layers, whose magnetization direction alternates between neighboring layers, forming an antiferromagnetic order. Besides surfaces with a magnetic gap, there also exsist gapless surfaces with a single Dirac cone, which can be gapped out when proximity coupled to an $s$-wave superconductor. On the sharing edges between the two types of gapped surfaces, the chiral Majorana modes emerge. We further propose experimental signatures of these Majoana hinge modes in terms of two-terminal conductance measurements.

*Introduction.*— Majorana edge mode, appearing as a gapless excitation on the boundary of a topological superconductor (TSC), has attracted a lot of attention because of its unusual property in analogy to the theoretically proposed Majorana fermion in particle physics, which is its own antiparticle [1–4]. The zero dimensional version of Majorana modes are zero-energy excitations localized at the ends of a 1D TSC, and thus give rise to degenerate many-body ground states, which can be used as nonlocal qubits and memory for quantum computing [5–7]. Engineering Majorana zero modes in a variety of systems has been proposed theoretically [8–13] and tested experimentally [14–25].

The 1D chiral Majorana mode (CMM) is a unidirectionally propagating mode appearing on the boundary of a 2D $p \pm ip$ chiral superconductor [26], which has a full pairing gap in the bulk and can be regarded as the superconducting analog of a Chern insulator. The propagation of the 1D CMMs has been shown in Ref. [27] to give rise to the similar qubic operations as Majorana zero modes do, enabling performing quantum computation with CMMs.

On the experimental side, the CMMs were proposed to be realized in a heterostructure comprising a quantum anomalous Hall insulator (QAHI) and an $s$-wave superconductor [28–31]. Based on this proposal, it was reported in a recent experiment [32] that the CMM was observed via a transport measurement of $e^2/2h$ conductance plateau in a QAHI-TSC-QAHI junction formed with a Cr-doped $(Bi, Sb)_2Te_3$ thin films in proximity with a Nb superconductor.

However, the interpretation of this conductance plateau as a signature for the presence of CMMs is under debate. In this experiment, an external magnetic field is required to tune the thin film into a magnetization reversal stage, when the system is near a QAHI-normal insulator phase transition [32]. It is expected that the system in this magnetization reversal stage is extremely inhomogeneous, which leads to alternative explanations of the conductance plateau under strong disorders without CMMs [33–35].

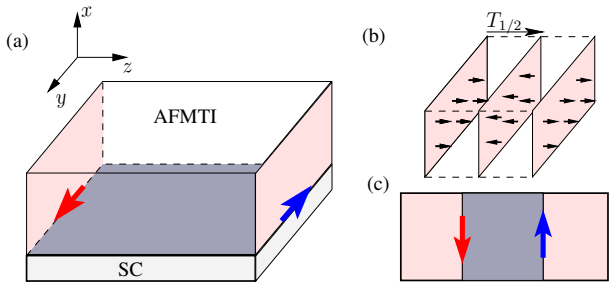


Figure 1. (a) Majorana hinge modes (blue and red arrows) at the edge of the interface (in grey) between an AFMTI and an $s$-wave SC. The antiferromagnetic ordering and the magnetization direction are both assumed to be along $z$ direction. We also assume the left and right surfaces (in pink) to have opposite magnetization. (b) The AFMTI can be regarded as magnetic layers, which are ferromagnetically ordered within each layer, and antiferromagnetically ordered between layers. (c) Effective description of the left-bottom-right surfaces of the AFMTI, in which the hinge modes appears at the domain wall between magnetic gapped (pink) and superconducting gapped (grey) regions.

In this Letter, we propose to realize CMMs on the hinges of a 3D antiferromagnetic topological insulator (AFMTI) (Fig. 1(a)), which was first introduced in Ref. [36] by studying model Hamiltonians. The advantage of this proposal is that no additional magnetic proximity/fields is required and superconductivity is introduced via the proximity effect by coupling to a conventional $s$-wave superconductor. Moreover, there are already material candidates for the AFMTI thanks to the

recent works [37–39] predicting that the tetradymite-type $MnBi_2Te_4$-related ternary chalgogenides ($MB_2T_4$: M = transition-metal or rare earth element, B = Bi or Sb, T = Te, Se or S) are presumable AFMTIs. In particular, $MnBi_2Te_4$ as a AFMTI has been experimentally confirmed [39, 40].

Our proposal is based on the simple picture that the surface state of a time-reversal invariant topological insulator (TRITI) in proximity with an $s$-wave superconductor resembles a $p \pm ip$ superconductor [8]. The surface of the TRITI does not have a boundary by itself. However, at the interfaces between such a surface $p \pm ip$ superconductor and a TRITI surface gapped out by a time-reversal breaking term, which may be realized by coupling to a magnetic insulator, the CMMs emerge.

An AFMTI can be regarded as a TRITI with a staggered time-reversal breaking potential adiabatically switched on without band gap closing. The system then acquires a layered structure with antiferromagnetic order between layers and ferromagnetic order within the layers, as schematically shown in Fig. 1(b). The ferromagnetic surfaces (pink surfaces in Fig. 1(a)) have gapped surface states similar to the one on a TRITI surface coupled to a magnetic insulator. There are also surfaces (grey surface in Fig. 1(a)) with zero net magnetization, which host a single Dirac cone and can be gapped out in proximity with an $s$-wave superconductor. On the sharing hinges between the two types of gapped surfaces, the CMMs should appear as indicated in red and blue arrows in Figs. 1(a,c). Note that the propagating direction of the CMM is determined by the surface magnetization direction and the relative orientation between the two types of surfaces.

It is worth mentioning that by combining the AFMTI with the conventional $s$-wave superconductor, we actually are able to realize a 3D higher-order topological superconductor [41–46], which belongs to a class of recently discovered topological phase with a gapped bulk and gapless boundary modes living in at least two dimensions lower.

In the following, we will first recall the basic properties of an AFMTI, with the help of a tight-binding AFMTI model, first introduced in Ref. [36]. We then show that the CMMs appear as one introduces superconductivity on the gapless AFMTI surfaces. We further propose experimental signatures of these CMMs in terms of transport measurements.

*AFMTI recap.*— 3D insulators with broken time-reversal $\Theta$ can have topological nontrivial features similar to that of the TRITI, if the symmetry due to $\mathcal{S} = \Theta T_{1/2}$ is preserved [36], where $T_{1/2}$ is a primitive lattice translation symmetry that is broken by the antiferromagnetic order, as illustrated in Fig. 1(b). One important difference between the AFMTI and the TRITI is that not all surfaces are gapless. Indeed, the surfaces are gapless only when they preserve the bulk symmetry $\mathcal{S}$. The surface is called type F (ferromagnetic) if it breaks $\mathcal{S}$ symmetry, while it is called type A (antiferromagnetic) if it preserves $\mathcal{S}$ [36]. For example, in Fig. 1(a), the top, bottom, front and back surfaces of the AFMTI are of type A which give rise to gapless surface states, whereas the left and right are type F surfaces with gapped surface states.

The AFMTI can be viewed as a TRITI with additional staggered time-reversal breaking terms [36], such as antiferromagnetically ordered layers of magnetic moments as shown in Fig. 1(b). This picture was recently demonstrated by *ab initio* calculations of materials such as $MnBi_2Te_4$ [37, 38]. In $MnBi_2Te_4$, the staggered magnetic potential that breaks the time-reversal symmetry is generated by the Mn atoms, while topological states are introduced by the Bi-Te layers similar as in $Bi_2Te_3$ [47]. It was reported that the states close to the Fermi level are $p$-bands of Bi/Te, and the Mn $d$-bands are far away from the band gap with an extremely large exchange splitting ($> 7$eV) [37].

In order to make the following discussion simple, rather than staying with real materials, we adopt the tight-binding model for AFMTI developed in Ref. [36] based on the above intuition, which captures all essential (topological) properties of a realistic AFMTI.

The model is constructed from a four-band TRITI model defined on a cubic lattice (lattice constant equals to 1) with the following Bloch Hamiltonian [48]

$$\mathcal{H}_{\mathrm{TI}}(k_x, k_y, k_z) = m\rho_z + \sum_{j=x,y,z} (t \cos k_j \rho_z + \lambda \sin k_j \sigma_j \rho_x), \tag{1}$$

where $\sigma_j$ and $\rho_j$ ($j = x, y, z$) are two sets of Pauli matrices for spin and orbital degrees of freedom. The time-reversal symmetry in this system is realized by $-i\sigma_y\mathcal{K}$, with complex conjugation $\mathcal{K}$. Note that the system is a strong topological insulator for $|m| \in (|t|, 3|t|)$ with finite spin-orbit coupling ($\lambda \neq 0$). To have an AFMTI, we further introduce a staggered exchange field alternating between $V$ and $-V$ in neighboring layers along the $(\bar{1}\bar{1}1)$ direction, which develops an antiferromagnetic order. We denote the Bloch Hamiltonian of this AFMTI as $\mathcal{H}(\mathbf{k})$, whose explicit form is given in Supplemental Material [49]. In general, $V$ is required to break time-reversal symmetry, and we choose $V = M\sigma_z$ without loss of generality.

In the antiferromagnetic state, the unit cell contains two sublattices $A$ and $B$, which feel the exchange potential $V$ and $-V$, respectively. Let us choose $A$ and $B$ sites at positions $(0, 0, 0)$ and $(0, 0, 1)$, with respect to the original cubic lattice vectors $\hat{\mathbf{x}}, \hat{\mathbf{y}}, \hat{\mathbf{z}}$. The new lattice vectors for the enlarged antiferromagnetic unit cell can be chosen as $\mathbf{a}_1 = \hat{\mathbf{x}} + \hat{\mathbf{z}}$, $\mathbf{a}_2 = \hat{\mathbf{y}} + \hat{\mathbf{z}}$, and $\mathbf{a}_3 = 2\hat{\mathbf{z}}$. In this model, the $(\bar{1}\bar{1}1)$ surface parallel to $\mathbf{a}_1, \mathbf{a}_2$ is type F, while the (100) surface parallel to $\mathbf{a}_2, \mathbf{a}_3$ is type A (same as the (010) surface). The bulk and surface band structures along these terminations are shown in Figs. 2(a) and (b), in which

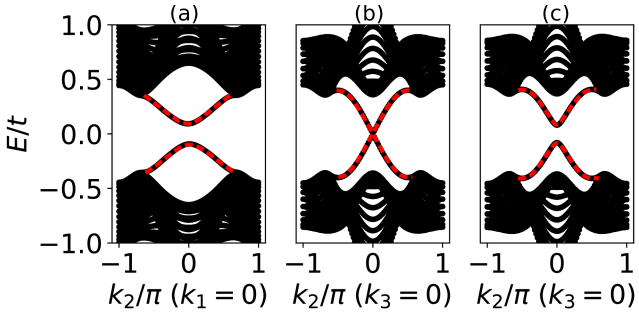


Figure 2. Bulk and surface band structures for AFMTI, along the (a) $(\bar{1}\bar{1}1)$ and (b,c) (100) surfaces, in which we fixed one momentum ($k_1$ or $k_3$) to zero. (c) is the BdG band structure when superconducting pairing potential $\Delta/t = 0.1$ was introduced at the surfaces, which decays exponentially into the bulk along $\mathbf{a}_1$ with decaying length $\xi = 3$. The surface states are indicated by red dashed lines. The other parameters are $\lambda/t = 0.5$, $m/t = 2$, $M/t = 1.2$ with 18 unit cells along the finite direction.

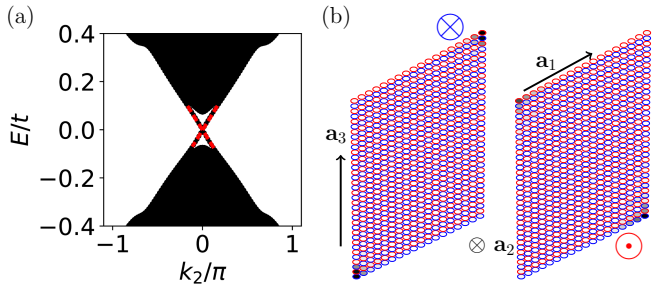


Figure 3. (a) Bulk and hinge band structure for the proximity coupled AFMTI, with periodic boundary condition along $\mathbf{a}_2$ ($k_2$ is well defined). The other parameters are the same as in Fig. 2(c). The hinge states are indicated by red dashed lines. (b) Norm of the hinge state wave functions at $k_2 = 0$ as a function of positions. The blue and red circles denote the $A$ and $B$ sites. The blackness inside the circles indicate the magnitude of the wave function norm. Left: One of the doubly degenerate CMMs propagating inward, along $\mathbf{a}_2$. Right: One of the doubly degenerate CMMs propagating outward, along $-\mathbf{a}_2$. The numbers of layers along $\mathbf{a}_1$ and $\mathbf{a}_3$ are 18 and 36 (18 for A and 18 for B), respectively.

we introduced $k_j = \mathbf{k}\cdot\mathbf{a}_j$ with Bloch momenta $\mathbf{k}$, and we find that the surface states of type F and type A surfaces are indeed gapped and gapless, respectively.

*Surface states.*— The gapped surface states on type F surfaces can be imagined as the surface Dirac cone of a TRITI gapped out by a magnetic potential, similar to the situation when a TRITI surface proximity coupled to a magnetic insulator [8]. On the other hand, the gapless surface states on type A surfaces can be gapped out when proximity coupled to an $s$-wave superconductor such as Nb. This creates intraorbital $s$-wave pairing $\Delta = \langle c^\dagger_{A,\mathbf{k}\uparrow\beta} c^\dagger_{A,-\mathbf{k}\downarrow\beta}\rangle = \langle c^\dagger_{B,\mathbf{k}\uparrow\beta} c^\dagger_{B,-\mathbf{k}\downarrow\beta}\rangle$, whose strength decays exponentially into the bulk. Here $c^\dagger_{X,\mathbf{k}\sigma\beta}$ ($X$=$A$,$B$, $\sigma$ =$\uparrow,\downarrow$, $\beta = 1,2$) creates an electron at sublattice $X$ in orbital $\beta$ with momentum $\mathbf{k}$ and spin $\sigma$.

The Bloch Bogoliubov–de Gennes (BdG) Hamiltonian for the AFMTI bulk with intraorbital $s$-wave pairing potential has the following form

$$\mathcal{H}_{\rm BdG} = \begin{pmatrix} \mathcal{H}(\boldsymbol{k}) & -i\Delta\sigma_y \\ i\Delta\sigma_y & -\mathcal{H}(-\boldsymbol{k})^* \end{pmatrix}. \qquad (2)$$

To show that type A surfaces of the AFMTI can indeed be gapped out via proximity effect, we consider a finite number of unit cells along $\mathbf{a}_1$, and choose the periodic boundary condition along $\mathbf{a}_2$ and $\mathbf{a}_3$, such that the momenta $k_2$ and $k_3$ are still well defined. By rewriting Eq. (2) in real space along $\mathbf{a}_1$ and taking a spatial dependent pairing potential $\Delta(n\mathbf{a}_1) = \Delta\exp(-n/\xi)$ decaying at length scale $\xi$, the BdG bulk and surface spectra along (100) planes can be calculated. The dispersion of the gapped surface states are shown in Fig. 2(c).

*Majorana hinge states.*— Recall that CMMs appear at the domain wall between two regions, obtained from gapping out a TRITI surface states by time-reversal breaking field and superconducting pairing potential, respectively [8]. In the proximity coupled AFMTI model introduced above, the common shared edges between type F and type A surfaces can be regarded as such domain walls, when surface superconductivity is introduced on type A surfaces.

To demonstrate such chiral Majorana hinge modes on these shared edges, let us assume the system is finite along $\mathbf{a}_1$ and $\mathbf{a}_3$, and periodic along $\mathbf{a}_2$. The superconducting proximity effect is modeled by introducing the intraorbital $s$-wave pairing potential which decays exponentially from the (100) surfaces into the bulk, described previously.

In Fig. 3(a), we show the bulk and hinge band structure, in which there are doubly gapless chiral modes propagating with positive and negative velocities, as indicated by red dashed lines. These gapless chiral states are indeed localized around the hinges shared by $(\bar{1}\bar{1}1)$ and (100) surfaces, which are the top/bottom and left/right edges in Fig. 3(b).

Note that when we have an even number of layers along $\mathbf{a}_3$, the top and bottom $(\bar{1}\bar{1}1)$ surfaces will carry opposite magnetization, which creates two CMMs with the same chirality located in a diagonal fashion with respect to each other, as shown in Fig. 3(b). The double degeneracy of the gapless modes is due to the two fold rotation symmetry with axis along $\mathbf{a}_2$, which relates the two diagonally aligned hinges along $\mathbf{a}_2$.

When we change the number of layers along $\mathbf{a}_3$ from even to odd, the magnetization of top surface and bottom $(\bar{1}\bar{1}1)$ surfaces points to the same direction. We still have four gapless CMMs, due to the four edges shared by $(\bar{1}\bar{1}1)$ and (100) surfaces. However, the two hinge modes with the same chirality will appear on the same side of the

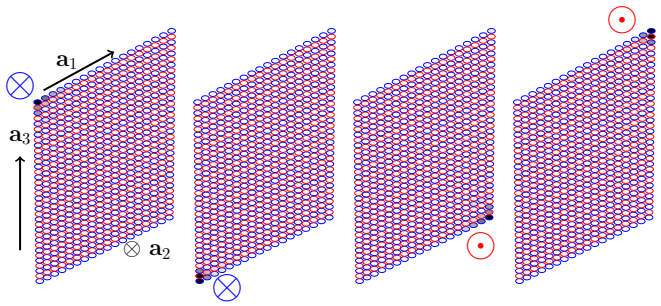


Figure 4. Norm of the four hinge state wave functions at $k_2 = 0$ as a function of positions. The blue and red circles denote the $A$ and $B$ sites. The blackness inside the circles indicate the magnitude of the wave function norm. The propagating directions of the modes are indicated by the symbol "$\otimes$" and "$\odot$" for along $\mathbf{a}_2$ and $-\mathbf{a}_2$. The numbers of layers along $\mathbf{a}_1$ and $\mathbf{a}_3$ are 18 and 35 (18 for A and 17 for B), respectively.

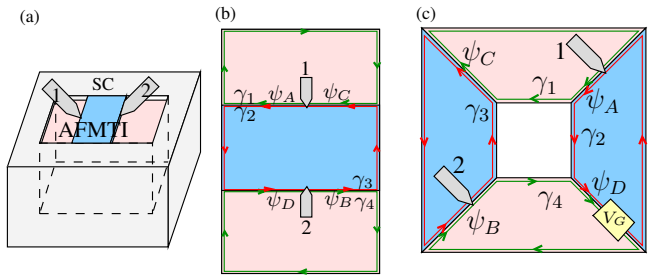


Figure 5. (a) Setup for transport measurement of the CMMs. The top surface of the AFMTI is type F, in which there is a region with opposite magnetization direction compared with the rest of the surface, as indicated with different colors. All type A surfaces sharing edges with the top surface are in proximity with the superconductor from the side. We connect leads 1,2 at the two domain walls between regions with opposite magnetizations. (b) The pattern of the chiral electron modes (double lines) and the CMMs (single lines) on the top surface, in which the arrows indicate propagating directions. (c) Setup up for measuring quantum coherence of CMMs, viewed from the top surface, in which the color indicates the magnetization direction. In the yellow region, a gate with voltage $V_G$ is added. The superconductor is proximity coupled to the outer and inner surfaces of the AFMTI from the side.

(100) surface, as shown in Fig. 4. Moreover, the two chiral CMMs with the same chirality will have slightly different velocities, due to lack of symmetry which relates one another.

Thus, by changing the number of layers along the antiferromagnetic order direction of the AFMTI, one is able to engineer the CMMs with desired propagating directions, which can be used, for example, to design a transport experiment detecting the CMMs, as discussed in the following.

*Experimental signature.*— To detect the CMMs at the hinges of the AFMTI, we propose a transport measurement based on the setup shown in Fig. 5(a), in which the AFMTI is surrounded by the $s$-wave superconductor, such that the top surface be type F, and all type A surfaces sharing edges with the top surface are in proximity with the superconductor. Moreover, we require the top surface to have a region in which the number of layers along the $T_{1/2}$ direction differs by one from that of the rest of the surface. Because of the antiferromagnetic ordering, this creates two domain walls between regions with different magnetizations on the top surface. Thus, we expect to have a single chiral electron modes on each of the domain walls, propagating in opposite directions [36, 37] (see Supplemental Material [49]). Furthermore, there are CMMs appearing on these sharing edges between the two types of surfaces. The propagating directions of these CMMs are determined by the magnetization direction, and the relative alignment between type F and type A surfaces.

In Fig. 5(b), we illustrate these chiral electron and Majorana modes in green and red lines on the edges of the top surface, with arrows indicating the their propagating directions. Note that the chiral electron mode are shown as (green and red) double lines given the fact that the chiral electron mode can be decomposed as two chiral CMMs. We further connect leads 1 and 2 to these two chiral electron modes, as illustrated in the figure, and measure the conductance $\sigma_{12}$ between them. We show in the following that $\sigma_{12} = \frac{e^2}{2h}$, same as the signature of CMM proposed in the QAHI-TSC-QAHI system [29, 32].

Let us denote the chiral electron mode flowing out from (into) leads 1 and 2 as $\psi_A$ and $\psi_B$ ($\psi_C$ and $\psi_D$). These modes can be decomposed into CMMs as $\psi_A = (\gamma_1 + i\gamma_2)/2$, $\psi_B = (\gamma_4 + i\gamma_3)/2$, $\psi_C = (\gamma_1 - i\gamma_3)/2$, $\psi_D = (\gamma_4 + i\gamma_2)/2$ [29]. Consider a scattering event by regarding $(\psi_A, \psi_A^\dagger, \psi_B, \psi_B^\dagger)$ as incident modes, and $(\psi_C, \psi_C^\dagger, \psi_D, \psi_D^\dagger)$ as outgoing modes, then the scattering matrix $\mathbf{S}$, which relates the incident modes and the outgoing modes, can be obtained (see Supplemental Material [49]). In particular, we find the probabilities for an incident electron from lead 1 in channel $\psi_A$ transmits into $\psi_C$ as an electron and into $\psi_C^\dagger$ as a hole are both 1/4, which leads to the two-terminal conductance $\sigma_{12} = \frac{e^2}{2h}$ according to the generalized Landauer formula [50].

It was mentioned in Ref. [27] that the half-quantized $\sigma_{12}$ does not reflect the quantum coherence of these CMMs. To find out the whether the CMMs are coherent or not, we follow this work and propose a similar setup based on AFMTI, as shown in Fig. 5(c), in which we add a gate with voltage $V_G$ in a region of the chiral electron mode $\psi_D = \gamma_4 + i\gamma_2$. This gate creates a term $H_G = V_G \psi_D^\dagger \psi_D$ within a length $l_G$ through which $\psi_D$ travels. This introduces a phase factor $\varphi_G = V_G l_G / v_F$ by $\psi_D \to \psi_D e^{-i\varphi_G}$, where $v_F$ is the Fermi velocity of $\psi_D$ under the gate. This leads to a phase-dependent two-terminal conductance $\sigma_{12} = (1 + \cos\varphi_G)e^2/2h$ [27] (see Supplemental Material [49]).

We further comment that the setup shown in Fig. 5 can also be used to show the braiding properties of the CMMs, similar to their zero-dimensional cousins [27]. Hopefully the device based on CMMs in AFMTI can be used as a platform for topological quantum computation.

*Conclusions.*— In this work, we showed that the CMMs can be realized on the hinges of a 3D AFMTI in proximity with a conventional $s$-wave superconductor in no need of external magnetic fields/materials. From another point of view, our proposal realizes an engineered 3D higher-order topological superconductor, making our work also valuable to the active field of higher-order topological phases. Moreover, we found that the CMMs in the AFMTI can be detected, and their coherence property can be measured, using two-terminal conductance measurements, similar to the ones in a QAHI-TSC-QAHI junction.

Another nice feature of the proposed system is that by engineering step edges on type F surfaces of the AFMTI, one is able to create a a network of chiral propagating electron and Majorana modes in a controlled fashion [36, 37]. This makes the AFMTI/superconductor platform an excellent candidate for topological quantum computing based on CMMs.

Given the very recent progresses in material discovery [37–40], such systems can presumably be realized using the $MnBi_2Te_4$-type AFMTI coupled with the $s$-wave superconductor (like Nb), making our proposal to a great extent accessible to experimentalists.

*Acknowledgments.*—Y.P. acknowledges support from the IQIM, an NSF physics frontier center funded in part by the Moore Foundation, and support from the Walter Burke Institute for Theoretical Physics at Caltech. Y.X. acknowledges support from the Basic Science Center Project of NSFC (Grant No. 51788104), the Ministry of Science and Technology of China (Grants No. 2018YFA0307100 and No. 2018YFA0305603), the National Thousand-Young-Talents Program and Tsinghua University Initiative Scientific Research Program.

* yangpeng@caltech.edu
† yongxu@mail.tsinghua.edu.cn

[1] M. Z. Hasan and C. L. Kane, Rev. Mod. Phys. **82**, 3045 (2010).
[2] X.-L. Qi and S.-C. Zhang, Rev. Mod. Phys. **83**, 1057 (2011).
[3] J. Alicea, Rep. Prog. Phys. **75**, 076501 (2012).
[4] C. Beenakker, Annu. Rev. Condens. Matter Phys. **4**, 113 (2013).
[5] A. Y. Kitaev, Ann. Phys. **303**, 2 (2003).
[6] C. Nayak, S. H. Simon, A. Stern, M. Freedman, and S. Das Sarma, Rev. Mod. Phys. **80**, 1083 (2008).
[7] D. Aasen, M. Hell, R. V. Mishmash, A. Higginbotham, J. Danon, M. Leijnse, T. S. Jespersen, J. A. Folk, C. M. Marcus, K. Flensberg, and J. Alicea, Phys. Rev. X **6**, 031016 (2016).
[8] L. Fu and C. L. Kane, Phys. Rev. Lett. **100**, 096407 (2008).
[9] R. M. Lutchyn, J. D. Sau, and S. Das Sarma, Phys. Rev. Lett. **105**, 077001 (2010).
[10] Y. Oreg, G. Refael, and F. von Oppen, Phys. Rev. Lett. **105**, 177002 (2010).
[11] S. Nadj-Perge, I. K. Drozdov, B. A. Bernevig, and A. Yazdani, Phys. Rev. B **88**, 020407 (2013).
[12] F. Pientka, L. I. Glazman, and F. von Oppen, Phys. Rev. B **88**, 155420 (2013).
[13] Y. Peng, F. Pientka, L. I. Glazman, and F. von Oppen, Phys. Rev. Lett. **114**, 106801 (2015).
[14] V. Mourik, K. Zuo, S. M. Frolov, S. Plissard, E. P. Bakkers, and L. P. Kouwenhoven, Science **336**, 1003 (2012).
[15] A. Das, Y. Ronen, Y. Most, Y. Oreg, M. Heiblum, and H. Shtrikman, Nat. Phys. **8**, 887 (2012).
[16] H. O. H. Churchill, V. Fatemi, K. Grove-Rasmussen, M. T. Deng, P. Caroff, H. Q. Xu, and C. M. Marcus, Phys. Rev. B **87**, 241401 (2013).
[17] M. Deng, C. Yu, G. Huang, M. Larsson, P. Caroff, and H. Xu, Nano Lett. **12**, 6414 (2012).
[18] A. Finck, D. Van Harlingen, P. Mohseni, K. Jung, and X. Li, Phys. Rev. Lett. **110**, 126406 (2013).
[19] S. Nadj-Perge, I. K. Drozdov, J. Li, H. Chen, S. Jeon, J. Seo, A. H. MacDonald, B. A. Bernevig, and A. Yazdani, Science **346**, 602 (2014).
[20] M. Ruby, F. Pientka, Y. Peng, F. von Oppen, B. W. Heinrich, and K. J. Franke, Phys. Rev. Lett. **115**, 197204 (2015).
[21] R. Pawlak, M. Kisiel, J. Klinovaja, T. Meier, S. Kawai, T. Glatzel, D. Loss, and E. Meyer, npj Quantum Inf. **2**, 16035 (2016).
[22] M. Deng, S. Vaitiekėnas, E. B. Hansen, J. Danon, M. Leijnse, K. Flensberg, J. Nygård, P. Krogstrup, and C. M. Marcus, Science **354**, 1557 (2016).
[23] S. M. Albrecht, A. Higginbotham, M. Madsen, F. Kuemmeth, T. S. Jespersen, J. Nygård, P. Krogstrup, and C. Marcus, Nature **531**, 206 (2016).
[24] M. Ruby, B. W. Heinrich, Y. Peng, F. von Oppen, and K. J. Franke, Nano Lett. **17**, 4473 (2017).
[25] Ö. Gül, H. Zhang, J. D. Bommer, M. W. de Moor, D. Car, S. R. Plissard, E. P. Bakkers, A. Geresdi, K. Watanabe, T. Taniguchi, *et al.*, Nat. Nanotechnol. , 1 (2018).
[26] N. Read and D. Green, Phys. Rev. B **61**, 10267 (2000).
[27] B. Lian, X.-Q. Sun, A. Vaezi, X.-L. Qi, and S.-C. Zhang, arXiv:1712.06156 (2017).
[28] X.-L. Qi, T. L. Hughes, and S.-C. Zhang, Phys. Rev. B **82**, 184516 (2010).
[29] S. B. Chung, X.-L. Qi, J. Maciejko, and S.-C. Zhang, Phys. Rev. B **83**, 100512 (2011).
[30] G. Strübi, W. Belzig, M.-S. Choi, and C. Bruder, Phys. Rev. Lett. **107**, 136403 (2011).
[31] J. Wang, Q. Zhou, B. Lian, and S.-C. Zhang, Phys. Rev. B **92**, 064520 (2015).
[32] Q. L. He, L. Pan, A. L. Stern, E. C. Burks, X. Che, G. Yin, J. Wang, B. Lian, Q. Zhou, E. S. Choi, *et al.*, Science **357**, 294 (2017).
[33] W. Ji and X.-G. Wen, Phys. Rev. Lett. **120**, 107002 (2018).
[34] Y. Huang, F. Setiawan, and J. D. Sau, Phys. Rev. B **97**, 100501 (2018).

[35] B. Lian, J. Wang, X.-Q. Sun, A. Vaezi, and S.-C. Zhang, Phys. Rev. B **97**, 125408 (2018).

[36] R. S. K. Mong, A. M. Essin, and J. E. Moore, Phys. Rev. B **81**, 245209 (2010).

[37] J. Li, Y. Li, S. Du, Z. Wang, B.-L. Gu, S.-C. Zhang, K. He, W. Duan, and Y. Xu, arXiv:1808.08608 (2018).

[38] D. Zhang, M. Shi, D. Xing, H. Zhang, and J. Wang, arXiv:1808.08014 (2018).

[39] M. M. Otrokov, I. I. Klimovskikh, H. Bentmann, A. Zeugner, Z. S. Aliev, S. Gass, A. U. B. Wolter, A. V. Koroleva, D. Estyunin, A. M. Shikin, M. Blanco-Rey, M. Hoffmann, A. Y. Vyazovskaya, S. V. Eremeev, Y. M. Koroteev, I. R. Amiraslanov, M. B. Babanly, N. T. Mamedov, N. A. Abdullayev, V. N. Zverev, B. Bchner, E. F. Schwier, S. Kumar, A. Kimura, L. Petaccia, G. Di Santo, R. C. Vidal, S. Schatz, K. Kiner, C.-H. Min, S. K. Moser, T. R. F. Peixoto, F. Reinert, A. Ernst, P. M. Echenique, A. Isaeva, and E. V. Chulkov, arXiv:1809.07389 (2018).

[40] Y. Gong, J. Guo, J. Li, K. Zhu, M. Liao, X. Liu, Q. Zhang, L. Gu, L. Tang, X. Feng, D. Zhang, W. Li, C. Song, L. Wang, P. Yu, X. Chen, Y. Wang, H. Yao, W. Duan, Y. Xu, S.-C. Zhang, X. Ma, Q.-K. Xue, and K. He, arXiv:1809.07926.

[41] W. A. Benalcazar, B. A. Bernevig, and T. L. Hughes, Science **357**, 61 (2017).

[42] Y. Peng, Y. Bao, and F. von Oppen, Phys. Rev. B **95**, 235143 (2017).

[43] J. Langbehn, Y. Peng, L. Trifunovic, F. von Oppen, and P. W. Brouwer, Phys. Rev. Lett. **119**, 246401 (2017).

[44] W. A. Benalcazar, B. A. Bernevig, and T. L. Hughes, Phys. Rev. B **96**, 245115 (2017).

[45] Z. Song, Z. Fang, and C. Fang, Phys. Rev. Lett. **119**, 246402 (2017).

[46] F. Schindler, A. M. Cook, M. G. Vergniory, Z. Wang, S. S. Parkin, B. A. Bernevig, and T. Neupert, Sci. Adv. **4**, eaat0346 (2018).

[47] H. Zhang, C.-X. Liu, X.-L. Qi, X. Dai, Z. Fang, and S.-C. Zhang, Nat. Phys. **5**, 438 (2009).

[48] P. Hosur, S. Ryu, and A. Vishwanath, Phys. Rev. B **81**, 045120 (2010).

[49] Supplemental Material.

[50] Y. Takane and H. Ebisawa, J. Phys. Soc. Jpn. **61**, 1685 (1992).

## SUPPLEMENTAL MATERIAL

## TIGHT-BINDING MODEL FOR AN AFMTI

In this section, we follow Ref. [36] and explicitly construct the tight-binding model for the AFMTI from the TRITI whose Bloch Hamiltonian is given by Eq. (1) in the main text. After introducing a staggered exchange field, which alternates between $V$ and $-V$ in neighboring layers along the $(\bar{1}\bar{1}1)$ direction, the unit cell contains two sites $A$ and $B$, which feel the exchange potential $V$ and $-V$ respectively.

Let us choose $A$ and $B$ sites at positions $(0,0,0)$ and $(0,0,1)$, with respect to the original cubic lattice vectors $\hat{\mathbf{x}},\hat{\mathbf{y}},\hat{\mathbf{z}}$. We can then define the new basis vectors $\mathbf{a}_1=\hat{\mathbf{x}}+\hat{\mathbf{z}}$, $\mathbf{a}_2=\hat{\mathbf{y}}+\hat{\mathbf{z}}$, and $\mathbf{a}_3=2\hat{\mathbf{z}}$ for the enlarged unit cell after introducing the staggered exchange field.

The onsite potentials on the $A$ and $B$ sites are

$$H_A=m\rho_z+V,\quad H_B=m\rho_z-V, \tag{1}$$

respectively. The hopping terms

$$T_{\pm x}=(t\rho_z\pm i\lambda\rho_x\sigma_x)/2 \tag{2}$$
$$T_{\pm y}=(t\rho_z\pm i\lambda\rho_x\sigma_y)/2 \tag{3}$$
$$T_{\pm z}=(t\rho_z\pm i\lambda\rho_x\sigma_z)/2 \tag{4}$$
$$\tag{5}$$

connect site $A$ to its six nearest neighbors of site $B$ along $\pm\hat{\mathbf{x}}$, $\pm\hat{\mathbf{y}}$ and $\pm\hat{\mathbf{z}}$ directions, respectively.

In terms of the basis vectors $\mathbf{a}_1$, $\mathbf{a}_2$ and $\mathbf{a}_3$, the above hopping terms translate into coupling within the same unit cell $H^0_{AB}=T_{-z}$, and various of hopping terms between neighboring unit cells $H^{\mathbf{a}_1}_{AB}=T_x$, $H^{\mathbf{a}_1-\mathbf{a}_3}_{AB}=T_{-x}$, $H^{\mathbf{a}_2}_{AB}=T_y$, $H^{\mathbf{a}_2-\mathbf{a}_3}_{AB}=T_{-y}$, and $H^{\mathbf{a}_3}_{AB}=T_z$, where $H^{\mathbf{d}}_{AB}$ denotes the vector $\mathbf{d}$ denotes the relative position of the involved two unit cells.

Let $\mathbf{k}$ be the Bloch momentum and $k_j=\mathbf{k}\cdot\mathbf{a}_j$ $(j=1,2,3)$, then the Bloch Hamiltonian of this system can be written as

$$\mathcal{H}(\mathbf{k})=(m\rho_z+M\sigma_z)\,\mu_z+\mathcal{V}(\mathbf{k})[\cos(k_3/2)\mu_x-\sin(k_3/2)\mu_y], \tag{6}$$

with

$$\mathcal{V}(\mathbf{k})=\left[\cos(k_1-\frac{k_3}{2})+\cos(k_2-\frac{k_3}{2})+\cos(\frac{k_3}{2})\right]\rho_z-\lambda\left[\sin(k_1-\frac{k_3}{2})\sigma_x+\sin(k_2-\frac{k_3}{2})\sigma_y+\sin\frac{k_3}{2}\sigma_z\right]\tau_x, \tag{7}$$

where we have introduced Pauli matrices $\mu_i$ $(i=x,y,z)$ for the sublattice degrees of freedom.

## CHIRAL ELECTRON MODES ON THE DOMAIN WALL OF THE AFMTI

Due to the antiferromagnetic order in the AFMTI, the magnetization direction of type F surface alternates as we change the number of layers along the antiferromagnetic direction. The step edge between regions with layer numbers differ by one can be regarded as a domain wall, on which the massive Dirac field changes its sign. Thus, a chiral electron mode is expected on this step edge [36]. In the following, we show this chiral electron mode in the tight-binding AFMTI model, as well as the coexisting chiral Majorana modes.

Let us take the previous introduced AFMTI model, and assume the system is finite along $\mathbf{a}_1$ and $\mathbf{a}_3$, and periodic along $\mathbf{a}_2$. We further assume there is a step edge along $\mathbf{a}_2$, on one of the type F surfaces parallel to $\mathbf{a}_1$ and $\mathbf{a}_2$, as shown in Fig. 6(a). The proximity-induced superconductivity is introduced by hand by adding a pairing potential $\Delta$, which decays exponentially into the bulk at a length scale $\xi$, on the left and right surfaces parallel to $\mathbf{a}_2$ and $\mathbf{a}_3$.

Since the system is periodic along $\mathbf{a}_2$, one can go to the momentum space and compute the BdG band structure as a function of the corresponding momentum $k_2$, as shown in Fig. 6(b). We actually obtain six chiral modes inside the bulk gap. Among these gapless modes, two of them correspond to a chiral electron mode localized at the step edge, whose wave functions at $k_2=0$ are shown in Figs. 6(c,d). The rest four are chiral Majorana modes localized at the outer four hinges of the AFMTI, with wave functions at $k_2=0$ shown in Figs. 6(e–h).

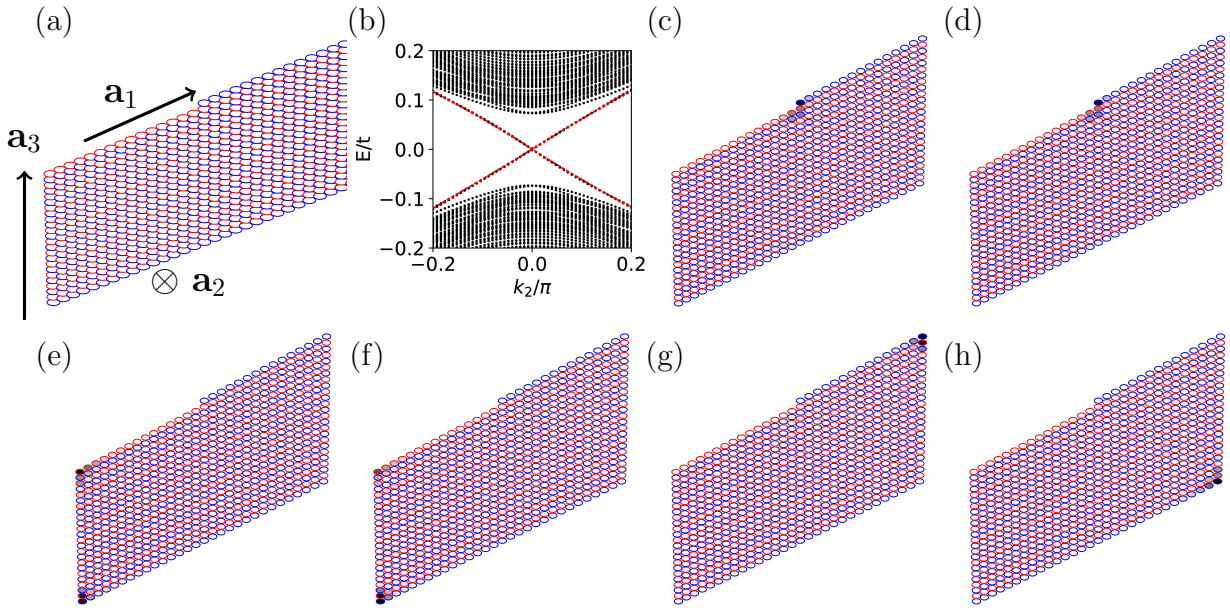


Figure 6. AFMTI with a step edge along $\mathbf{a}_2$ on one of tht type F surfaces parallel to $\mathbf{a}_1$ and $\mathbf{a}_2$. The system is finite along the directions of $\mathbf{a}_1$ and $\mathbf{a}_3$, and periodic in $\mathbf{a}_2$. The blue and red circles denote the $A$ and $B$ sites. (b) Bulk and hinge (including the step edge) band structure for the AFMTI, in which the left and right surfaces parallel to $\mathbf{a}_2$ and $\mathbf{a}_3$ are gapped out by proximity-induced superconducivity, with a pairing potential exponentially decaying into the bulk. The gapless hinge states (electron or Majorana modes) are indicated in red. (c–h) Norm of the hinge state wave functions at $k_2 = 0$ as a function of positions. The blackness inside the circles indicate the magnitude of the wave function norm. (c,d) Chiral electron modes (doubled in BdG Hamiltonian) on the step edge. (e-h) Four chiral Majorana modes on the four outer hinges. The parameters are $\Delta/t = 0.1$, $\lambda/t = 0.5$, $m/t = 2$, $M/t = 1.2$, $\xi = 3$. The system contains 30 layers along $\mathbf{a}_1$, and 24 or 25 layers along $\mathbf{a}_3$.

## SIGNATURES OF CHIRAL MAJORANA MODES IN TERMS OF TWO-TERMINAL CONDUCTANCE

In this section, we provide more details on the calculation of the two-terminal conductance $\sigma_{12}$.

Let us first consider the setup in Fig. 5(b) of the main text. One can imagine the system as a normal-superconductor-normal junction with chiral electron modes flowing out from (into) leads 1 and 2 are $\psi_A$ and $\psi_B$ ($\psi_C$ and $\psi_D$), which can be decomposed into chiral Majorana modes as $\psi_A = (\gamma_1 + i\gamma_2)/2$, $\psi_B = (\gamma_4 + i\gamma_3)/2$, $\psi_C = (\gamma_1 - i\gamma_3)/2$, $\psi_D = (\gamma_4 + i\gamma_2)/2$ [29]. Because of this decomposition, we have

$$\begin{pmatrix} \psi_C \\ \psi_C^\dagger \\ \psi_D \\ \psi_D^\dagger \end{pmatrix} = \mathbf{S} \begin{pmatrix} \psi_A \\ \psi_A^\dagger \\ \psi_B \\ \psi_B^\dagger \end{pmatrix}, \quad \mathbf{S} = \frac{1}{2} \begin{pmatrix} 1 & 1 & -1 & 1 \\ 1 & 1 & 1 & -1 \\ 1 & -1 & 1 & 1 \\ -1 & 1 & 1 & 1 \end{pmatrix}, \tag{8}$$

where $\mathbf{S}$ is the scattering matrix.

The two-terminal conductance is given by generalized Landauer formula [50]

$$\sigma_{12} = \frac{g_{11}g_{22} - g_{12}g_{21}}{g_{11} + g_{22} + g_{12} + g_{21}} \tag{9}$$

where

$$g_{ij} = \frac{e^2}{h}(\delta_{ij} - \left|S_{ij}^{ee}\right|^2 + \left|S_{ij}^{eh}\right|^2), \tag{10}$$

with $i, j = 1, 2$ corresponding to the lead label, and $S_{ij}^{\alpha\beta}$ ($\alpha, \beta = e, h$) is the matrix element of $\mathbf{S}$, in which the basis is ordered as $(1e, 1h, 2e, 2h)$. Using the scattering matrix $\mathbf{S}$, we have $g_{11} = g_{22} = e^2/h$ and $g_{12} = g_{21} = 0$. Thus, $\sigma_{12} = e^2/2h$.

This conductance can also be obtained in the following way [27]. Let us use $|n_X n_Y\rangle$ to denote an eigenstate of the occupation operators of modes $\psi_X, \psi_Y$, with eigenvalues $n_X, n_Y$ ($X, Y = A, B, C, D$). If we consider one electron

coming from from lead 1 or 2, then the system is prepared in state $|1_A 0_B\rangle$ or $|0_A 1_B\rangle$, which translates into a linear combination of the basis state in the outgoing channel via

$$\begin{pmatrix} |1_C 0_D\rangle \\ |0_C 1_D\rangle \end{pmatrix} = \mathcal{M} \begin{pmatrix} |1_A 0_B\rangle \\ |0_A 1_B\rangle \end{pmatrix}, \quad \mathcal{M} = \frac{1}{\sqrt{2}} \begin{pmatrix} 1 & -1 \\ 1 & 1 \end{pmatrix} \tag{11}$$

Hence, we see the probability of finding the electron incident from lead 1 or 2 is given by $|\langle 0_C 1_D | 1_A 0_B\rangle|^2 = 1/2$, giving rise to a conductance of $e^2/2h$.

To compute the two-terminal conductance $\sigma_{12}$ in Fig. 5(c) of the main text, we make use of the above approach by considering an incident electron coming from lead 1 or 2, namely we prepare the system in $|1_A 0_B\rangle$ or $|0_A 1_B\rangle$. We can imagine the electron propagation in this system in terms of two steps. First, the incident electron propagates into modes $\psi_C$ and $\psi_D$ (left top and right bottom of Fig. 5(c)) after experiencing the gate voltage $V_G$, which transforms $|0_C 1_D\rangle \to e^{-i\varphi_G} |0_C 1_D\rangle$. In the second step, the electron propagates back into modes $\psi'_A$ and $\psi'_B$, where $\psi'_A$ and $\psi'_B$ denote the outgoing modes into leads 1 and 2. The whole process can be described by the following transformation

$$\begin{pmatrix} |1_{A'} 0_{B'}\rangle \\ |0_{A'} 1_{B'}\rangle \end{pmatrix} = \mathcal{M}\mathcal{V}\mathcal{M} \begin{pmatrix} |1_A 0_B\rangle \\ |0_A 1_B\rangle \end{pmatrix}, \quad \mathcal{V} = \begin{pmatrix} 1 & 0 \\ 0 & e^{-i\varphi_G} \end{pmatrix}. \tag{12}$$

The conductance is thus given by

$$\sigma_{12} = \frac{e^2}{h} |\langle 0_{A'} 1_{B'} | 1_A 0_B\rangle|^2 = \frac{1 + \cos\varphi_G}{2} \frac{e^2}{h}. \tag{13}$$